Lasing in hybrid metal-Bragg nanocavities

Jong-Bum You,† Kyungmook Kwon,† Wook-Jae Lee, Jaeho Shim, Dongshik Won, Youngho Jung, Byounghun Park, and Kyoungsik Yu*

Department of Electrical Engineering, KAIST, Daejeon 305-701, South Korea
**Corresponding author: ksyu@kaist.edu*

Received February 22, 2013; revised April 3, 2013; accepted April 15, 2013;
posted April 16, 2013 (Doc. ID 185030); published May 13, 2013

We report room-temperature lasing from an optically pumped subwavelength-scale cylindrical InGaAsP pillar surrounded by circular Bragg reflectors on a metal substrate with a dielectric spacer layer. By taking advantage of wide in-plane photonic bandgaps and proper vertical antiresonances, three dielectric Bragg pairs produce a sufficient optical feedback capable of low threshold lasing from the fundamental TE_{011} mode. A large spontaneous emission coupling into the lasing mode is obtained from the cavity-enhanced Purcell effects and effective suppression of nonlasing modes. © 2013 Optical Society of America

OCIS codes: (140.3410) Laser resonators; (260.3910) Metal optics; (230.1480) Bragg reflectors; (140.5960) Semiconductor lasers.
http://dx.doi.org/10.1364/OL.38.001694

Photonic bandgap (PBG) resonator structures have attracted considerable interest as promising candidates for miniaturized light emitting devices. Examples include one-dimensional distributed Bragg reflectors (DBRs) [1], two-dimensional photonic crystal slabs [2], and circular Bragg reflectors (CBRs) [3]. Their high quality factor (Q) and small effective modal volume (V_{eff}) can greatly improve the laser threshold gain (g_{th}) [4], cavity quantum electrodynamic effects [5], and modulation speed [6]. However, the realization of ultrahigh Q/V_{eff} ratios typically requires large device footprints, which is an important limitation for dense photonic integration. Suspended membrane structures might also lead to poor thermal and mechanical reliabilities.

One possible way of resolving those challenges is to use metallodielectric (MD) resonator structures [7]. This approach can shrink the laser size into a small physical volume below one cubic wavelength [8,9]. However, few demonstrations are capable of room-temperature (RT) operation [10,11], because metal losses cannot readily be avoided and impose inevitable trade-offs with V_{eff} in the resonator design. There have also been efforts to combine the metal and PBG structures such as vertical metal-DBRs [12] and plasmonic crystals [13]. Although these approaches are well suited for miniaturizing the physical and/or modal volumes, they are either still bulky or require cryogenic cooling due to large metallic dissipation.

In this Letter, by combining in-plane CBRs and a metal reflector, we propose a hybrid approach to overcome practical challenges of PBG and MD structures: a large device footprint and the metal-induced threshold increase. We show that only three pairs of CBRs (even with low index contrast with SiO_2 cladding) are sufficient to realize a low threshold lasing from the subwavelength-scale cylindrical pillar at RT by taking advantage of a wide in-plane PBG and vertical antiresonances from the metal substrate. A large spontaneous emission (SE)-coupling factor can be obtained with nondegenerate single-mode operation based on the cavity-enhanced Purcell effects on the dominant cavity mode.

Figure 1(a) schematically shows the proposed structures consisting of a core cylindrical pillar (InGaAsP material with a diameter of $d = \sim 390$ nm and a height of $h = 350$ nm) surrounded by three pairs of CBRs made of the same material. They are embedded in SiO_2 cladding and the distance from the bottom metal (Ag) plane is $t = 300$ nm. The low and high refractive indices of 1.44 (SiO_2) and 3.4 (InGaAsP with a width of w) are periodically alternated along the radial direction. For device fabrication, the semiconductor gain medium is grown on an InP substrate. The pillar and Bragg reflector patterns are defined by electron beam lithography and reactive ion etching, and then multiple surface oxidation and oxide removal steps remove etching-induced surface damages [Fig. 1(b)]. The outer diameter of the largest ring is <3 μm. The silicon oxide layer was deposited by plasma-enhanced chemical vapor deposition with relatively low step coverage, resulting in a ~300 nm-thick spacer layer with a nearly flat top surface, and followed by electron beam evaporation of a ~2.5 μm-thick Ag layer. The samples were then flipped and bonded to a silicon substrate, and the InP substrate was finally removed [14].

Complete rotational symmetry can support strong omnidirectional reflections toward the core region from the CBRs. In particular, the in-plane PBG for the transverse electric (TE) polarization is desired for larger Bragg reflections due to its broad forbidden region, which can be widened by reducing the filling factor (ff, InGaAsP width w over the Bragg pitch a) of the CBRs. The target ff is determined to be ~0.3 for fabrication reliability. The lasing mode (TE_{011}, the fundamental

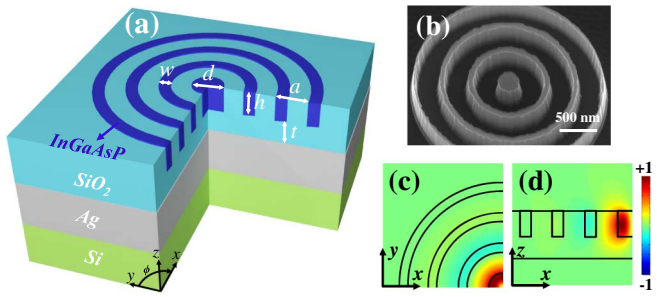

Fig. 1. (a) Schematic layout of the proposed cavity. (b) A representative scanning electron micrograph of the cavity structure (InGaAsP material) prior to depositing the SiO_2 cladding. (c) In-plane and (d) out-of-plane electric field (E_ϕ) profiles for the lasing mode (TE_{011}).

TE mode with the azimuthal mode number of 0) is highly confined around the core pillar region [Figs. 1(c) and 1(d)]. However, such strong in-plane localization inevitably leads to weak vertical confinement due to diffraction losses [15]. In order to overcome such problems, we incorporate a metal substrate acting as a mirror, located properly apart from the PBG slab to induce vertical antiresonances [16].

We performed three-dimensional (3D) finite-difference time domain (FDTD) analysis to understand the cavity resonance properties. Figure 2(a) shows the resonant frequencies of the upper and lower band edge resonances (TE polarization) and the cavity resonance (TE_{011}) as a function of a for $d = 390$ nm. The field profiles (E_ϕ) show that the antinodes for the lower and upper band edge modes are mainly located within the high and low index regions, respectively [insets of Fig. 2(a)], while the cavity mode is dominantly confined in the core region [Fig. 1(c)].

We also investigate the cavity confinement by decomposing the calculated total quality factor (Q_{tot}) into three contributions : $1/Q_{tot} = 1/Q_{in} + 1/Q_{out} + 1/Q_{abs}$, where Q_{in}, Q_{out}, and Q_{abs} are due to in-plane and out-of-plane radiation losses and metal absorption losses, respectively, as shown in Fig. 2(b). The low ff of 0.3 widens the PBG width for TE polarization with the gap to mid-gap ratio of up to 0.63. For example, this wide PBG can achieve threefold enhancement of Q_{tot} compared with $ff = 0.5$. When the TE_{011} resonance is positioned around the PBG center, the cavity mode can be highly localized with the lowest V_{eff} of ~0.37 $(\lambda_0/n)^3$, and its resonant frequency becomes close to the RT SE peak. Q_{in} is also maximized due to strong lateral confinement. Because of the vertical antiresonances, relatively high Q_{out} is obtained despite the strong Bragg reflection. Our simulations confirm that the optimum vertical antiresonances are obtained with $t = \sim 300$ nm and $h = \sim 350$ nm (the corresponding phase thickness of $\sim 0.56\pi$ and $\sim 0.92\pi$, respectively) for the cavity resonance at ~1550 nm [16]. Note that the presence of the metal substrate can actually improve Q_{out} over ~20 times greater than that of the CBR structures with the SiO_2 substrate for the Bragg period of 440 ~ 460 nm. We also obtain very high Q_{abs} exceeding 10^4, which is an order of magnitude higher than Q_{tot}. Finally, high theoretical Q_{tot} can be achieved with a broad range of a from 400 to 500 nm, which allows low threshold gain below

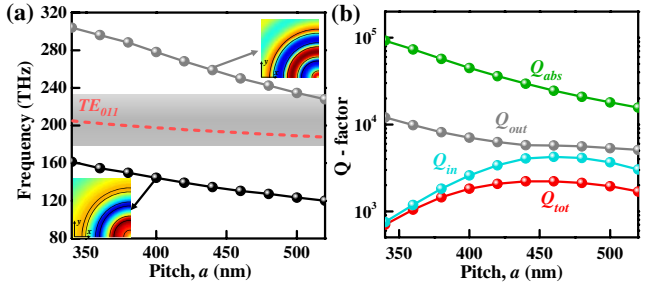

Fig. 2. Simulated cavity properties for $d = 390$ nm, $h = 350$ nm, $t = 300$ nm, and $ff = 0.3$. (a) Resonant frequencies of TE-polarized band edge resonances and cavity resonance (TE_{011}) as a function of the period, a. The shaded region indicates the gain bandwidth. The insets show electric field (E_ϕ) profiles of the band edge modes. (b) Decomposed Q-factors as a function of a for TE_{011}.

100 cm^{-1} (e.g., $g_{th} \sim 83$ cm^{-1} for $a = 440$ nm) suited for RT operation [10, 17].

Another distinct feature of our resonator design is that the strong cavity-enhanced SE occurs for the single lasing mode within the wide spectral range. In contrast, other nonlasing modes (e.g., TM or hybrid modes such as HE or EH) cannot be supported with reasonable quality factors using only a few CBR pairs, and the role of metal for such modes is also minor. These interesting properties are confirmed by computing the SE enhancement ($\gamma_{cavity}/\gamma_{bulk}$, ratio of cavity to bulk SE rate) [18] and the SE coupling factor (β, ratio between the SE rate into a mode of interest and into all modes) [19]. The SE enhancement can be written as follows:

$$\frac{\gamma_{cavity}}{\gamma_{bulk}} = \sum_i \left(F_i \frac{\Delta f_i^2}{4(f - f_i)^2 + (\Delta f_i)^2} \right).$$

F_i is the effective Purcell factor including the spatial and polarization mismatches of field and dipoles (randomly distributed in the core pillar) of the ith mode with the center frequency of f_i and the linewidth of Δf_i. Because of the mismatches, F_i is typically much smaller than the Purcell factor for an ideal single emitter $[F_p = 6Q(\lambda_0/2n)/(\pi^2 V_{eff})]$.

The SE enhancement spectra are obtained from 3D FDTD simulations and shown in Fig. 3 for several Bragg pitches. These results prove that there is a clear cavity-enhanced SE for the lasing mode, while most nonlasing modes cannot enhance the SE rate beyond the bulk SE level. Furthermore, the metal effects on the spontaneous photon emission rate for the nonlasing modes are relatively small due to their coupling with lossy surface waves with poor confinements. This is confirmed by comparing the SE enhancement with and without the metal substrate, as shown in Fig. 3. These comparisons imply that the benefits from the metal substrate are mostly absent for the nonlasing modes and only applicable to the lasing mode with high Purcell effects. The importance of such discrimination is signified by large theoretical values of $F = 35$ and $\beta = 0.412$ for the lasing mode (TE_{011}) with $a = 440$ nm and $Q_{tot} = \sim 2200$.

The experimental lasing characteristics are shown in Fig. 4. For measurements, the sample is optically pumped at RT using a 1064 nm semiconductor laser with 20 ns pulse width and 100 kHz repetition rate. The pump beam

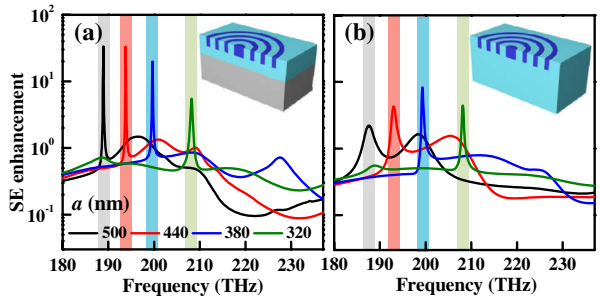

Fig. 3. SE enhancement for (a) the proposed hybrid metal-CBR structures and (b) the CBR structures with the SiO_2 substrate (Bragg pitch $a = 500$, 440, 380, and 320 nm for $d = 390$ nm, $h = 350$ nm, $t = 300$ nm, and $ff = 0.3$). The TE_{011} modes are highlighted by color bands.

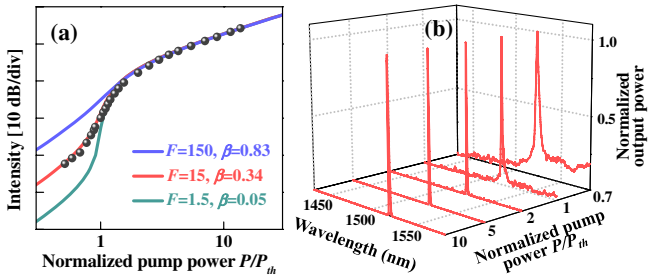

Fig. 4. (a) Logarithmic plots of experimental (circles) and theoretical (solid lines) output light intensity. (b) Evolution of the output emission spectra when the pump power varies from 0.7 to $10\times P_{\text{th}}$. The measured device dimensions are $d = \sim 390$ nm, $a = \sim 440$ nm, $t = \sim 300$ nm.

is focused to the beam waist diameter of ~1.9 μm using an objective lens (numerical aperture 0.5), which also collects the output emission from the samples. We confirm that the lasing mode is actually TE_{011} by observing the donut-shaped radiation pattern, which is consistent with the theoretical predictions. The pump absorption efficiency and energy confinement factor in the core region are estimated to be ~4% and ~70%, respectively. According to our calculations, 32% of the lasing mode output can be captured by the objective lens, while 38% goes to the SiO_2 cladding and 7% is dissipated in metal.

Around the lasing threshold, the irradiated peak pump power is measured to be 270 μW. The experimentally observed emission wavelength of 1520 nm and the total quality factor of ~1130, which corresponds to $g_{\text{th}} \sim 165\ \text{cm}^{-1}$, are different from the theoretical values mainly due to the imperfect sidewall slope. A linewidth of ~0.9 nm (close to the resolution limit of our spectrometer) was obtained at $\sim 3\times P_{\text{th}}$. We observe single-mode emission from a broad range of wavelengths below threshold as expected from the theoretical predictions of SE in Fig. 3(a). The measured L-L curve (circles) with a typical S-shaped behavior is compared with fitted curves (solid lines) for various F and β values obtained from the simplified rate equations to model the dynamics of carrier and photon densities, and pump power [7]. The measured f and Δf for the lasing mode near threshold are incorporated into the rate equation model, while F is adjusted to fit the measured curve ($F < F_p$). Since contributions from the nonlasing modes to the overall SE rate are not significant and less sensitive to geometries, FDTD simulation results are used in the rate equation model. Nonradiative surface recombination lifetime of ~1 ns is obtained from the typical RT surface recombination velocity of 10^4 cm/s [20]. The radiative recombination coefficient of $B = 3\times 10^{-10}\ \text{cm}^3\,\text{s}^{-1}$ is assumed in the model. As a result, the rate equation curve is best fitted with the F and the corresponding β of ~15 and ~0.34, respectively, which are in good agreement with the theoretical results ($F = \sim 18$, $\beta = \sim 0.38$) when considering the decrease of the quality factor from ~2200 to ~1130.

In summary, we demonstrate low-threshold RT single-mode lasing from a subwavelength-scale pillar surrounded by a few Bragg reflector pairs and a metal substrate. Even with an ultracompact cavity structure and low index contrast, our hybrid approach achieves strong lateral and vertical confinement by employing the wide in-plane PBG and vertical antiresonances. Moreover, the SE and its coupling to the lasing mode (TE_{011}) are greatly enhanced by the single-mode operation and effective suppression of nonlasing low-Q modes. We believe that the proposed approach enables integrated nanolasers with small device footprints and low lasing thresholds for a number of applications.

This research was supported by Basic Science Research Program through the National Research Foundation of Korea (NRF) and the Center for Integrated Smart Sensors as Global Frontier Project funded by the Ministry of Education, Science and Technology (2008-0662256, 2010-0002845, CISS-2011-0031864).

†The first two authors contributed equally to this work.

References

1. J. L. Jewell, J. P. Harbison, A. Scherer, Y. H. Lee, and L. T. Florez, IEEE J. Quantum Electron. **27**, 1332 (1991).
2. O. Painter, R. K. Lee, A. Scherer, A. Yariv, J. D. O'Brien, P. D. Dapkus, and I. Kim, Science **284**, 1819 (1999).
3. J. Scheuer, W. M. J. Green, G. A. DeRose, and A. Yariv, Appl. Phys. Lett. **86**, 251101 (2005).
4. M. Lončar, T. Yoshie, A. Scherer, P. Gogna, and Y. Qiu, Appl. Phys. Lett. **81**, 2680 (2002).
5. T. Yoshie, A. Scherer, J. Hendrickson, G. Khitrova, H. M. Gibbs, G. Rupper, C. Ell, O. B. Shchekin, and D. G. Deppe, Nature **432**, 200 (2004).
6. S. Matsuo, A. Shinya, T. Kakitsuka, K. Nozaki, T. Segawa, T. Sato, Y. Kawaguchi, and M. Notomi, Nat. Photonics **4**, 648 (2010).
7. M. T. Hill, Y.-S. Oei, B. Smalbrugge, Y. Zhu, T. deVries, P. J. van Veldhoven, F. W. M. van Otten, T. J. Eijkemans, J. P. Turkiewicz, H. de Waardt, E. J. Geluk, S.-H. Kwon, Y.-H. Lee, R. Nötzel, and M. K. Smit, Nat. Photonics **1**, 589 (2007).
8. K. Yu, A. Lakhani, and M. C. Wu, Opt. Express **18**, 8790 (2010).
9. M. Khajavikhan, A. Simic, M. Katz, J. H. Lee, B. Slutsky, A. Mizrahi, V. Lomakin, and Y. Fainman, Nature **482**, 204 (2012).
10. M. P. Nezhad, A. Simic, O. Bondarenko, B. Slutsky, A. Mizrahi, L. Feng, V. Lomakin, and Y. Fainman, Nat. Photonics **4**, 395 (2010).
11. R. M. Ma, R. F. Oulton, V. J. Sorger, G. Bartal, and X. Zhang, Nat. Mater. **10**, 110 (2010).
12. C.-Y. Lu, S. L. Chuang, A. Mutig, and D. Bimberg, Opt. Lett. **36**, 2447 (2011).
13. A. M. Lakhani, M. Kim, E. K. Lau, and M. C. Wu, Opt. Express **19**, 18237 (2011).
14. K. Kwon, J.-B. You, J. Shim, W.-J. Lee, and K. Yu, *17th OptoElectronics and Communications Conference* (IEEE, 2012), pp. 297–298.
15. Y. Akahane, T. Asano, B. S. Song, and S. Noda, Nature **425**, 944 (2003).
16. S. H. Kim, J. Huang, and A. Scherer, J. Opt. Soc. Am. B **29**, 577 (2012).
17. E. O. Goebel, G. Luz, and E. Schlosser, IEEE J. Quantum Electron. **15**, 697 (1979).
18. Y. Xu, J. Vučković, R. K. Lee, O. Painter, A. Scherer, and A. Yariv, J. Opt. Soc. Am. B **16**, 465 (1999).
19. J. Vučković, O. Painter, Y. Xu, A. Yariv, and A. Scherer, IEEE J. Quantum Electron. **35**, 1168 (1999).
20. A. Forchel, A. Menschig, B. Maile, H. Leier, and R. Germann, J. Vac. Sci. Technol. B **9**, 444 (1991).